Electronic Supplementary Information

Construction of cluster-based supramolecular wire and rectangle

Yi Tan,[ab] Zhi-Kang Wang,[a] Fei-Fan Lang,[c] Hui-Min Yu,[a] Chen Cao,[a] Chun-Yan Ni,[a] Meng-Yi Wang,[d] Ying-Lin Song,[d] Jian-Ping Lang*[ab]

[a] *College of Chemistry, Chemical Engineering and Materials Science, Soochow University, Suzhou 215123, People's Republic of China. E-mail: jplang@suda.edu.cn; Fax: 86-512-65882865; Tel: +86-512-65880328*

[b] *State Key Laboratory of Organometallic Chemistry, Shanghai Institute of Organic Chemistry, Chinese Academy of Sciences, Shanghai 200032, People's Republic of China*

[c] *Department of Chemistry, University of Sheffield, Sheffield, United Kingdom*

[d] *School of Physical Science and Technology, Soochow University, Suzhou 215006, Jiangsu, People's Republic of China*

Table of contents

Single crystal X-ray structure determination S3

Table S1 Selected crystal data and structure refinement for **2**·1.6$CHCl_3$, **3**·1.4DMF·CH_2Cl_2, **4**, and **5**..... S4

Fig. S1 Electronic spectra of **L2-L4** (1×10^{-5} M) in DMF in a 1 cm-thick cuvette. S7

Fig. S2 Solid-state optical absorbance spectra of **2-5** derived from diffuse reflectance data S7

Fig. S3 (a) The positive-ion ESI mass spectrum of **3**. (b) The observed patterns (up) and the calculated isotope patterns (bottom) of the $[Tp^*WS_3Cu(\mathbf{L2})(Et_2O)(MeCN)_2(H)]^+$ cation (at m/z = 1116.9739) in **3**. S8

Fig. S4 (a) The positive-ion ESI mass spectrum of **4**. (b) The observed patterns (up) and the calculated isotope patterns (bottom) of the $[Tp^*WS_3Cu_3Cl]^+$ cation (at m/z = 802.8226) in **4**. (c) The observed patterns (up) and the calculated isotope patterns (bottom) of the $[Tp^*WS_3Cu_3(MeOH)(OTf)]^+$ cation (at m/z = 957.8335) in **4**. (d) The observed patterns (up) and the calculated isotope patterns (bottom) of $[(Tp^*WS_3Cu_2Cl)_2(MeOH)(OTf)(H)_2]^+$ cation (at m/z = 1662.9046) in **4**. S9

Fig. S5 (a) The positive-ion ESI mass spectrum of **5**. (b) The observed patterns (up) and the calculated isotope patterns (bottom) of the $[Tp^*WS_3Cu_3Cl]^+$ cation (at m/z = 802.8221) in **5**. (c) The observed patterns (up) and the calculated isotope patterns (bottom) of the $[Tp^*WS_3Cu_3(MeOH)(OTf)]^+$ cation (at m/z = 957.8323) in **5**. (d) The observed patterns (up) and the calculated isotope patterns (bottom) of $[(Tp^*WS_3Cu_2Cl)_2(MeOH)(OTf)(H)_2]^+$ cation (at m/z = 1662.9026) in **5**. S10

Fig. S6 View of the intermolecular hydrogen bonding interactions C-H···Cl between two adjacent molecules of **2**. The lattice solvates, all the H atoms and Tp* groups are omitted for clarity. Color codes: W, red; Cu, cyan; S, yellow; Cl, dark green; N, blue; C, black; B, dark orange. S11

Fig. S7. (a) View of the structure of **4** with all H atoms omitted for clarity. Color codes: W, red; Cu, cyan; S, yellow; Cl, dark green; N, blue; C, black; B, dark orange. (b) View of the structure of **5** with all H atoms omitted for clarity. Color codes: W, red; Cu, cyan; S, yellow; Cl, dark green; N, blue; C, black; B, dark orange; O, Fuchsia. S11

Details for the third-order NLO measurements of 3-5 ..... S12

Fig. S8 *Z*-scan data for **4** (5×10^{-5} M) in DMF investigated at 532 nm. (a) Normalized *Z*-scan data obtained using an open-aperture configuration showing the nonlinear absorption. (b) Normalized *Z*-scan data obtained using a closed-aperture configuration showing the nonlinear refraction. The black solid spheres are the experimental data, and the red solid curves are the theoretical fits. S13

Fig. S9 *Z*-scan data for **5** (5×10^{-5} M) in DMF investigated at 532 nm. (a) Normalized *Z*-scan data obtained using an open-aperture configuration showing the nonlinear absorption. (b) Normalized *Z*-scan data obtained using a closed-aperture configuration showing the nonlinear refraction. The black solid spheres are the experimental data, and the red solid curves are the theoretical fits. S14

Single crystal X-ray structure determination

Single crystals of **2**·1.6$CHCl_3$, **3**·1.4DMF·CH_2Cl_2, **4**, and **5** suitable for X-ray analysis were obtained directly from the above preparations. Most of them were mounted with grease at the top of a glass fiber and cooled to 120 K in a liquid-nitrogen stream to be measured on a D8 VENTURE X-ray diffractometer with graphite-monochromated Mo Kα (λ = 0.71073 Å) radiation at 120 K, while one single crystal of **2**·1.6$CHCl_3$ was mounted on a Bruker D8-Quest CCD X-ray diffractometer with graphite-monochromated Mo Kα (λ = 0.71073 Å) radiation at 296.15 K. The collected data were reduced by the program *CrystalClear*, and an absorption correction (multi-scan) was applied. The reflection data for **2**·1.6$CHCl_3$, **3**·1.4DMF·CH_2Cl_2, **4**, and **5** were also corrected for Lorentz and polarization effects.

By using the full-matrix least-squares method in the SHELXL 2018 programs through the $OLEX^2$ interface,[S1] the crystal structures were solved by direct methods and refined on F^2. For **2**·1.6$CHCl_3$, the occupancy ratio of one $CHCl_3$ molecule was fixed to be 0.8 and these data over 50° were omitted from the refinement to get the relevant crystallographic parameters to a reasonable range. For **3**·1.4DMF·CH_2Cl_2, one OTf^- was treated as position disorder by applying PART 1 and PART 2 in the *.ins* file with the site occupation factors changed to 0.5 for the atoms. Meanwhile, one CH_2Cl_2 molecule with an occupancy factor of 0.5 in the asymmetric unit was split into two positions with an occupancy ratio of 0.35/0.15, and the occupancy ratios of two DMF molecule were fixed to be 0.4 and 0.3 to get the relevant crystallographic parameters to a reasonable range.

In addition, there is still a large amount of spatially delocalized electron density in the crystal lattice and it is difficult to meet the desired crystallographic parameters through refinement for **3**·1.4DMF·CH_2Cl_2, **4**, and **5**. Therefore the SQUEEZE procedure in PLATON[S2] was used to remove the remaining solvent contribution but it was very difficult to clearly assign solvent molecules of crystallization to the solvent mask. Furthermore, the large scattering ability of the heavy W atoms resulted in the high residual peaks for **4** (3.59 e/$Å^3$, 0.8964(5) Å from W) and **5** (2.34 e/$Å^3$, 0.9780(3) Å from W). The high disorder of the OTf^- anion also attributed to the residual Q peaks around one OTf^- anion in **3**·1.4DMF·CH_2Cl_2. The pertinent crystal data along with data collection and refinement parameters for **2**·1.6$CHCl_3$, **3**·1.4DMF·CH_2Cl_2, **4**, and **5** are summarized in Table S1, while their selected bond lengths are displayed in Table S2.

S1 O. V. Dolomanov, L. J. Bourhis, R. J. Gildea, J. A. K. Howard and H. Puschmann, *J. Appl. Crystallogr.*, 2009, **42**, 339-341.

S2 A. Spek, *J. Appl. Crystallogr.*, 2003, **36**, 7-13.

Table S1 Selected crystal data and structure refinement for **2**·1.6$CHCl_3$, **3**·1.4DMF·CH_2Cl_2, **4**, and **5**.

Compound	**2**·1.6$CHCl_3$	**3**·1.4DMF·CH_2Cl_2
Empirical formula	$C_{45.60}H_{53.60}B_2Cl_{6.80}Cu_4N_{16}S_8W_2$	$C_{113.20}H_{131.80}B_4Cl_8Cu_{12}F_6N_{29.40}O_{7.40}S_{14}W_4$
Formula weight	1966.86	4410.23
Crystal system	monoclinic	trigonal
Space group	$P2_1/n$	$P\bar{3}$
a/Å	16.8463(9)	26.3933(10)
b/Å	17.3053(10)	26.3933(10)
c/Å	12.4887(8)	25.7305(10)
α/°	90	90
β/°	113.8940(10)	90
γ/°	90	120
V/Å^3	3328.8(3)	15522.7(13)
Z	2	3
D_c/(gcm^{-3})	1.962	1.415
μ (Mo Kα)/mm^{-1}	5.267	3.710
F (000)	1914	6462
total reflns	42912	502820
unique reflns	5854	18220
no. of param	394	969
R_{int}	0.1021	0.1135
R_1[a]	0.0342	0.0537
wR_2[b]	0.0692	0.1369
GOF[c]	1.017	1.123

Compound	**4**	**5**
Empirical formula	$C_{106}H_{118}B_4Cl_6Cu_{12}F_6N_{30}O_6S_{14}W_4$	$C_{108}H_{116}B_4Cl_6Cu_{12}F_6N_{28}O_8S_{14}W_4$
Formula weight	4224.96	4250.94
Crystal system	triclinic	triclinic
Space group	$P\bar{1}$	$P\bar{1}$
a/Å	10.0436(7)	9.8327(7)
b/Å	18.5322(14)	16.2223(12)
c/Å	25.0944(18)	25.3788(17)
α/°	101.575(2)	91.961(2)
β/°	97.944(2)	91.493(2)
γ/°	97.164(2)	104.795(2)
V/Å^3	4475.6(6)	3909.1(5)
Z	1	1
D_c/(gcm^{-3})	1.568	1.806
μ (Mo Kα)/mm^{-1}	4.256	4.874
F (000)	2056	2068
total reflns	77776	46694
unique reflns	20542	13713
no. of param	859	868
R_{int}	0.1102	0.0736
R_1[a]	0.0677	0.0516
wR_2[b]	0.1694	0.1242
GOF[c]	1.036	1.036

5

[a] $R_1 = ||F_o|-|F_c||/|F_o|$. [b] $wR_2 = [w(F_o^2-F_c^2)^2/w(F_o^2)^2]^{1/2}$. [c] $GOF = \{w((F_o^2-F_c^2)^2)/(n-p)]\}^{1/2}$, where n = number of reflections and p = total numbers of parameters refined.

Table S2 Selected bond lengths (Å) for **2**, **3**[a], **4**[b], and **5**[c].

		Compound **2**	
W1···Cu2	2.6108(8)	W1···Cu1	2.6055(8)
W1–S2	2.3357(16)	W1–S3	2.2282(17)
W1–S1	2.2382(16)	W1–N6	2.262(5)
W1–N4	2.291(5)	W1–N2	2.287(5)
Cu2···Cu1	2.8118(11)	Cu2–S2	2.2209(19)
Cu2–S3	2.193(2)	Cu2–Cl1	2.1491(19)
Cu1–S2	2.1979(18)	Cu1–S1	2.1770(19)
Cu1–N7	1.926(5)		
		Compound **3**	
W1···Cu3	2.6306(11)	W1···Cu2	2.6553(11)
W1···Cu1	2.6444(12)	W1–S3	2.315(2)
W1–S1	2.301(2)	W1–S2	2.320(2)
W1–N10	2.277(7)	W1–N14	2.275(7)
W1–N12	2.283(7)	W2···Cu4	2.6536(13)
W2···Cu6	2.6504(12)	W2···Cu5	2.6417(13)
W2–S4	2.302(2)	W2–S5	2.311(3)
W2–S6	2.310(2)	W2–N2	2.254(8)
W2–N6	2.276(9)	W2–N4	2.289(8)
Cu3···Cu2	2.8959(15)	Cu3···Cu1	2.8948(16)
Cu3–S3	2.209(2)	Cu3–S2	2.207(2)
Cu3–N8	1.942(8)	Cu2···Cu1	2.8931(15)
Cu2–S3	2.233(3)	Cu2–Cl2$^{\#1}$	2.742(3)
Cu2–S1	2.220(2)	Cu2–Cl3$^{\#1}$	2.233(2)
Cu1–S1	2.222(2)	Cu1–S2	2.222(3)
Cu1–Cl1	2.220(3)	Cu4···Cu6	2.8919(17)
Cu4···Cu5	2.8660(17)	Cu4–Cl2	2.742(3)
Cu4–S4	2.231(3)	Cu4–S5	2.224(3)
Cu4–Cl3	2.239(3)	Cu6···Cu5	2.8773(18)
Cu6–Cl2	2.708(3)	Cu6–S4	2.221(3)
Cu6–S6	2.229(3)	Cu6–Cl1$^{\#1}$	2.231(3)
Cu5–Cl2	2.727(3)	Cu5–S5	2.219(3)
Cu5–S6	2.222(3)	Cu5–N7	1.935(9)
		Compound **4**	
W1···Cu6	2.6583(13)	W1···Cu4	2.6589(14)
W1···Cu5	2.6381(14)	W1–S1	2.323(3)
W1–S3	2.315(2)	W1–S2	2.303(3)
W1–N6	2.259(10)	W1–N4	2.273(9)
W1–N2	2.289(9)	W2···Cu1	2.6562(15)
W2···Cu3	2.6469(14)	W2–S5	2.305(3)
W2–S6	2.317(3)	W2–N13	2.265(10)
W2–N15	2.274(9)	W2–N11	2.276(11)
W2–S4	2.306(3)	W2···Cu2	2.6438(15)
Cu6···Cu4	2.8973(19)	Cu6···Cu5	2.9100(19)
Cu6–Cl2	2.695(3)	Cu6–S3	2.235(3)
Cu6–Cl1	2.230(3)	Cu6–S2	2.217(3)
Cu4···Cu5	2.8567(18)	Cu4–Cl2	2.761(3)

Cu4–S1	2.224(3)	Cu4–S2	2.234(3)
Cu4–Cl3$^{\#1}$	2.232(3)	Cu5–S1	2.215(3)
Cu5–S3	2.215(3)	Cu5–N7	1.954(9)
Cu1···Cu3	2.937(2)	Cu1–Cl2$^{\#1}$	2.706(3)
Cu1–Cl1$^{\#1}$	2.240(3)	Cu1–S5	2.227(3)
Cu1–S4	2.231(3)	Cu1···Cu2	2.890(2)
Cu3–S5	2.211(3)	Cu3–S6	2.196(3)
Cu3–N9	1.951(9)	Cu3···Cu2	2.9003(19)

Compound **5**

W2···Cu2	2.6533(10)	W2···Cu3	2.6738(10)
W2···Cu1	2.6462(11)	W2–S5	2.3037(18)
W2–S6	2.331(2)	W2–S4	2.3056(19)
W2–N4	2.283(6)	W2–N6	2.267(7)
W2–N2	2.261(6)	W1···Cu5	2.6383(11)
W1···Cu4	2.6516(9)	W1···Cu6	2.6510(10)
W1–S1	2.317(2)	W1–S2	2.325(2)
W1–S3	2.308(2)	W1–N12	2.278(7)
W1–N10	2.260(7)	W1–N14	2.258(7)
Cu5···Cu4	2.9396(15)	Cu5···Cu6	2.8708(14)
Cu5–S2	2.235(2)	Cu5–S3	2.230(2)
Cu5–Cl3	2.218(2)	Cu2···Cu3	2.8686(13)
Cu2···Cu1	2.8442(13)	Cu2–Cl2	2.642(2)
Cu2–S6	2.230(2)	Cu2–S4	2.238(2)
Cu2–N7	1.955(6)	Cu4···Cu6	2.9290(14)
Cu4–S1	2.211(2)	Cu4–S2	2.205(2)
Cu4–N8	1.926(6)	Cu3···Cu1	2.8964(14)
Cu3–S5	2.228(2)	Cu3–Cl2	2.637(2)
Cu3–S4	2.248(2)	Cu3–Cl3$^{\#1}$	2.250(2)
Cu6–Cl2$^{\#1}$	2.712(2)	Cu6–S1	2.247(2)
Cu6–S3	2.228(2)	Cu6–Cl1$^{\#1}$	2.251(2)
Cu1–S5	2.229(2)	Cu1–S6	2.231(2)
Cu1–Cl1	2.223(2)		

[a] Symmetry transformations used to generate equivalent atoms: #1: 1-*x*, 1-*y*, 2-*z*; [b] Symmetry transformations used to generate equivalent atoms: #1: 1-*x*, 1-*y*, 2-*z*; [c] Symmetry transformations used to generate equivalent atoms: #1: 1-*x*, 1-*y*, 1-*z*.

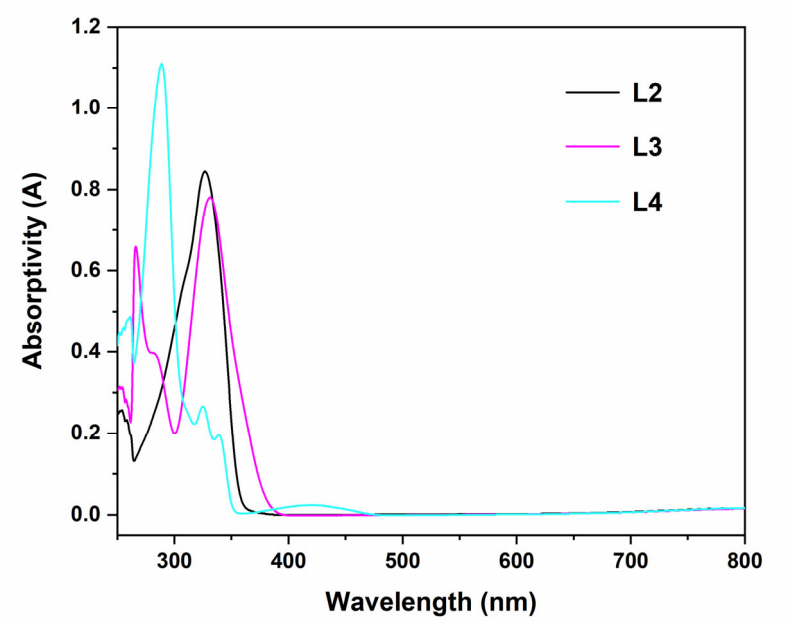

Fig. S1 Electronic spectra of **L2-L4** (1×10^{-5} M) in DMF in a 1 cm-thick cuvette.

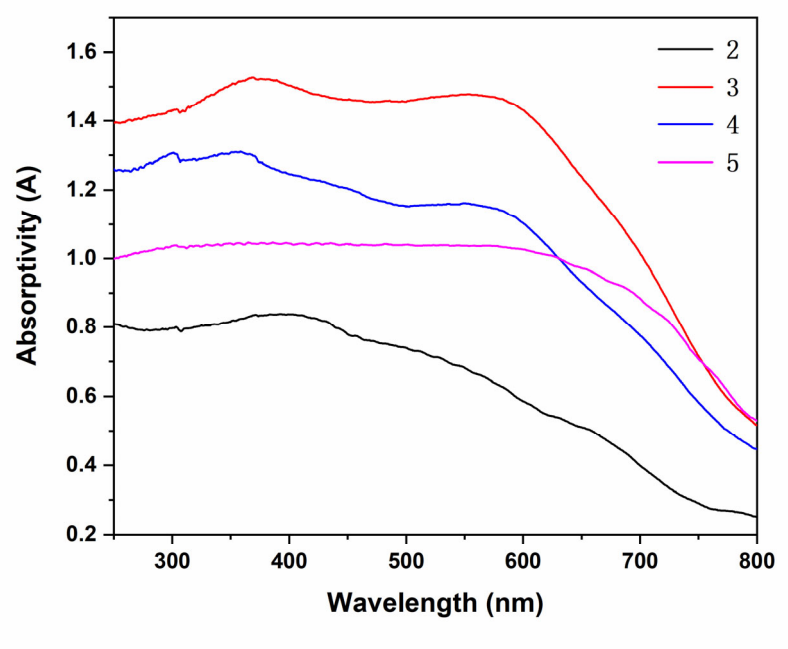

Fig. S2 Solid-state optical absorbance spectra of **2-5** derived from diffuse reflectance data

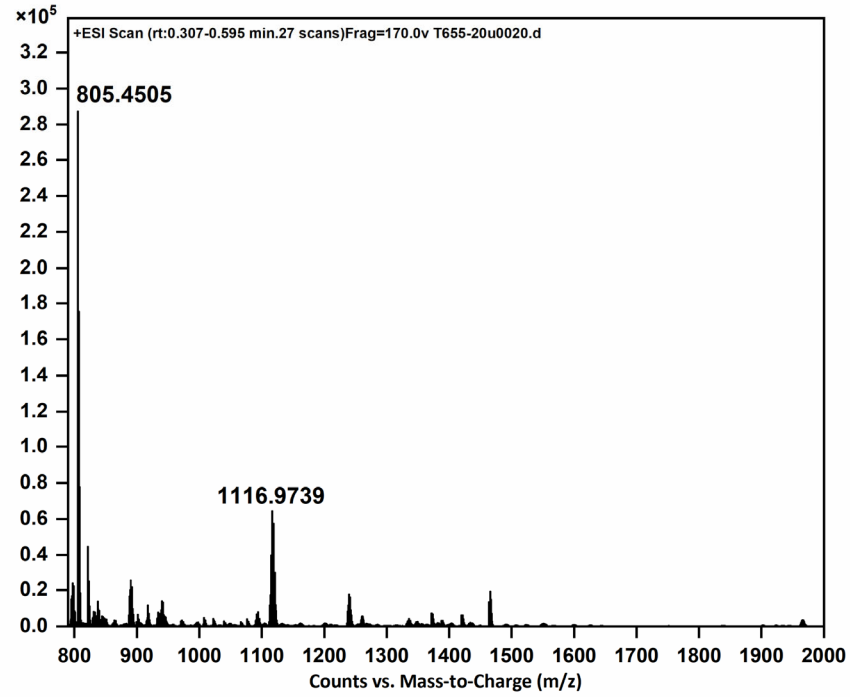

(a)

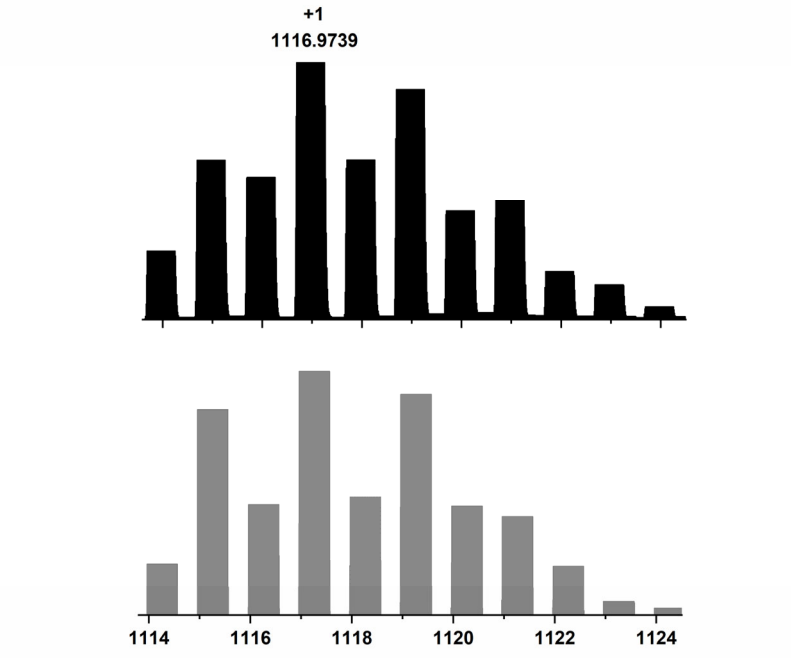

(b)

Fig. S3 (a) The positive-ion ESI mass spectrum of **3**. (b) The observed patterns (up) and the calculated isotope patterns (bottom) of the $[Tp^*WS_3Cu(\mathbf{L2})(Et_2O)(MeCN)_2(H)]^+$ cation (at m/z = 1116.9739) in **3**.

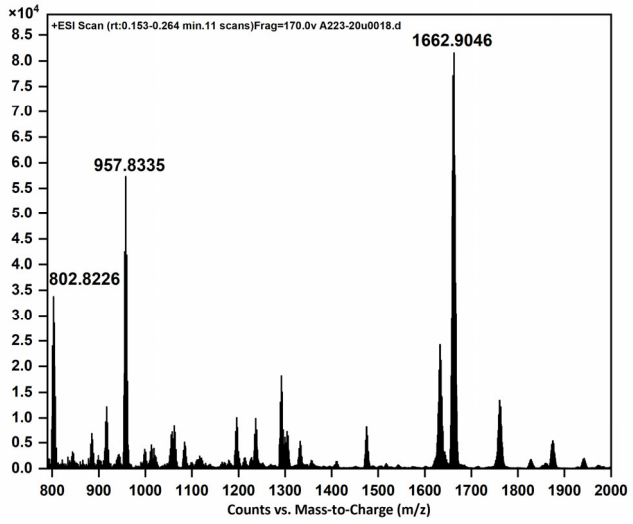

(a)

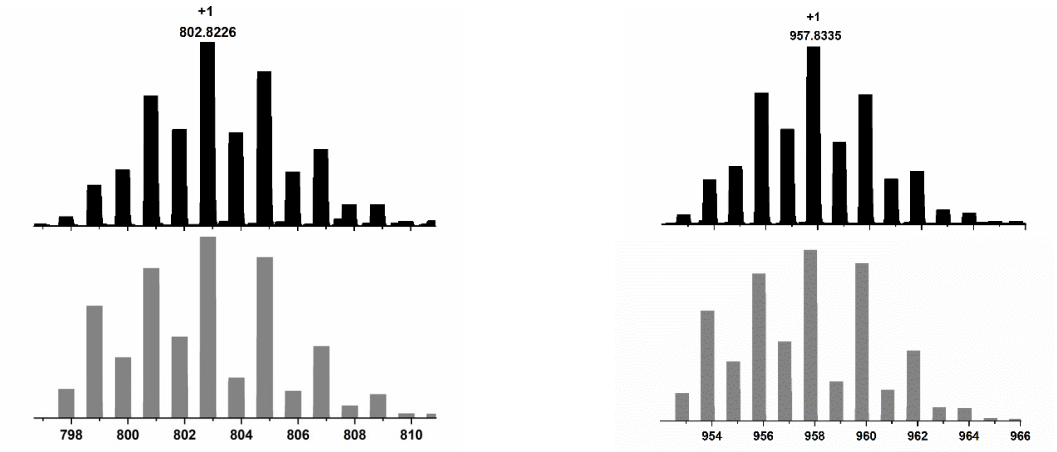

(b) (c)

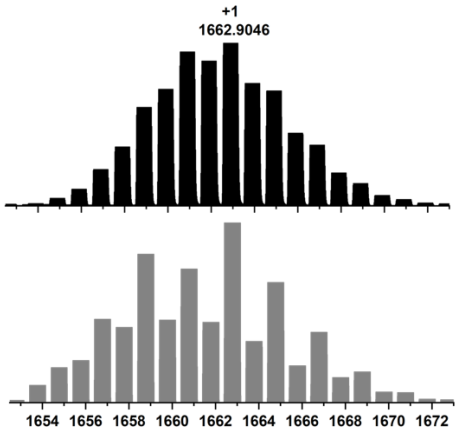

(d)

Fig. S4 (a) The positive-ion ESI mass spectrum of **4**. (b) The observed patterns (up) and the calculated isotope patterns (bottom) of the $[Tp^*WS_3Cu_3Cl]^+$ cation (at *m*/*z* = 802.8226) in **4**. (c) The observed patterns (up) and the calculated isotope patterns (bottom) of the $[Tp^*WS_3Cu_3(MeOH)(OTf)]^+$ cation (at *m*/*z* = 957.8335) in **4**. (d) The observed patterns (up) and the calculated isotope patterns (bottom) of $[(Tp^*WS_3Cu_2Cl)_2(MeOH)(OTf)(H)_2]^+$ cation (at *m*/*z* = 1662.9046) in **4**.

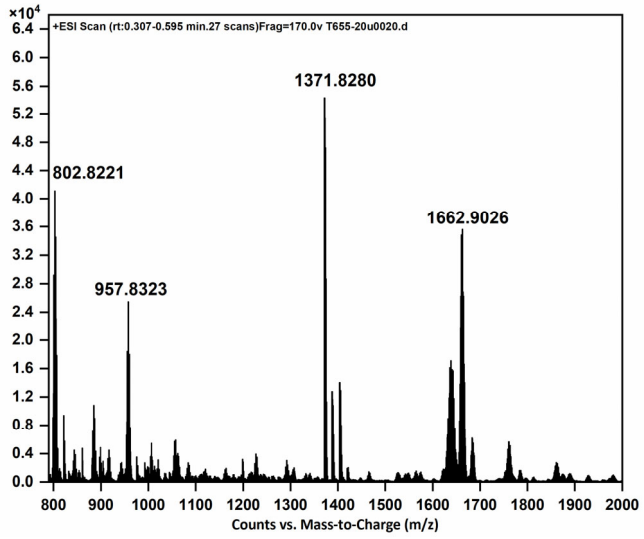

(a)

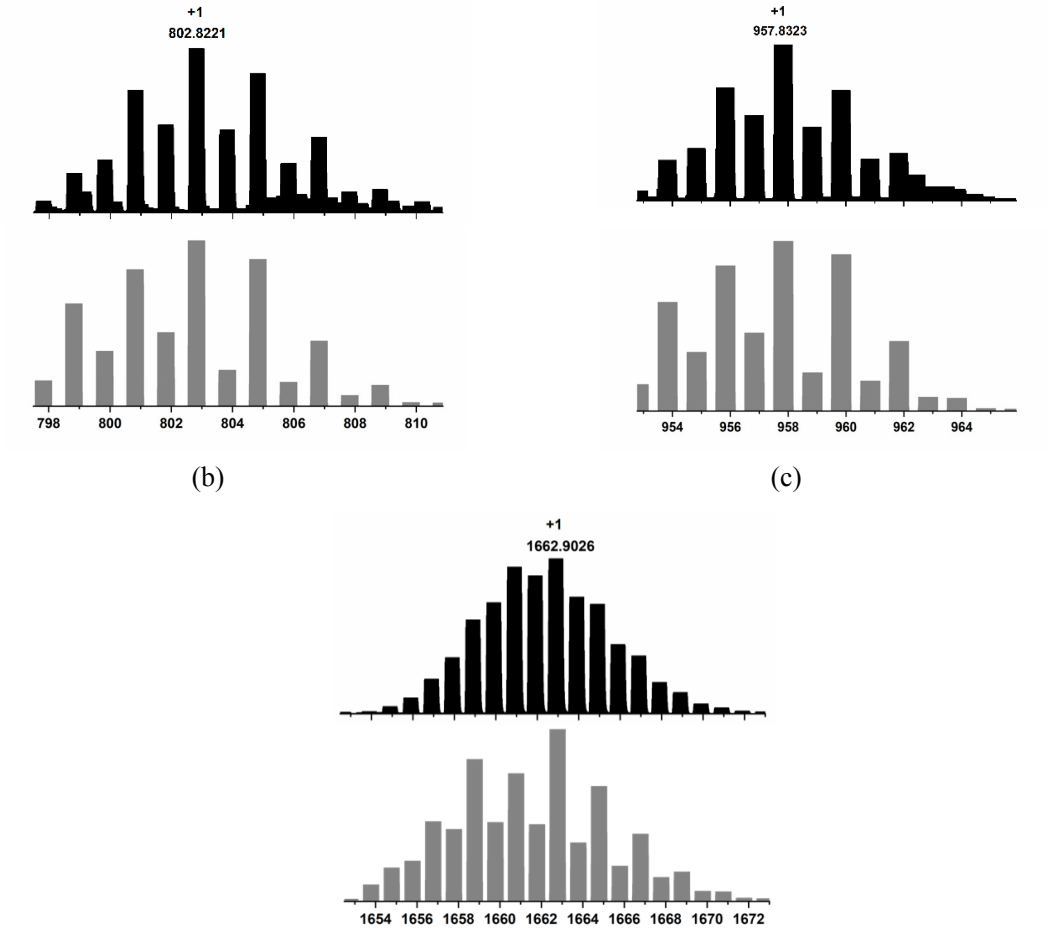

(b) (c)

(d)

Fig. S5 (a) The positive-ion ESI mass spectrum of **5**. (b) The observed patterns (up) and the calculated isotope patterns (bottom) of the $[Tp^*WS_3Cu_3Cl]^+$ cation (at m/z = 802.8221) in **5**. (c) The observed patterns (up) and the calculated isotope patterns (bottom) of the $[Tp^*WS_3Cu_3(MeOH)(OTf)]^+$ cation (at m/z = 957.8323) in **5**. (d) The observed patterns (up) and the calculated isotope patterns (bottom) of $[(Tp^*WS_3Cu_2Cl)_2(MeOH)(OTf)(H)_2]^+$ cation (at m/z = 1662.9026) in **5**.

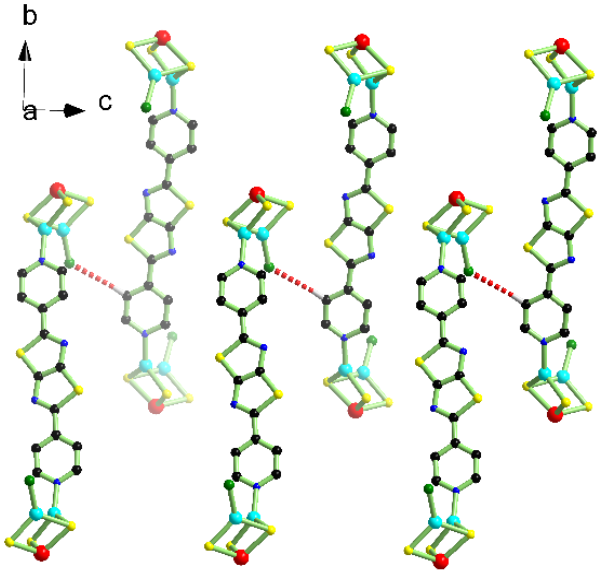

Fig. S6 View of the intermolecular hydrogen bonding interactions C-H···Cl between two adjacent molecules of **2**. The lattice solvates, all the H atoms and Tp* groups are omitted for clarity. Color codes: W, red; Cu, cyan; S, yellow; Cl, dark green; N, blue; C, black; B, dark orange.

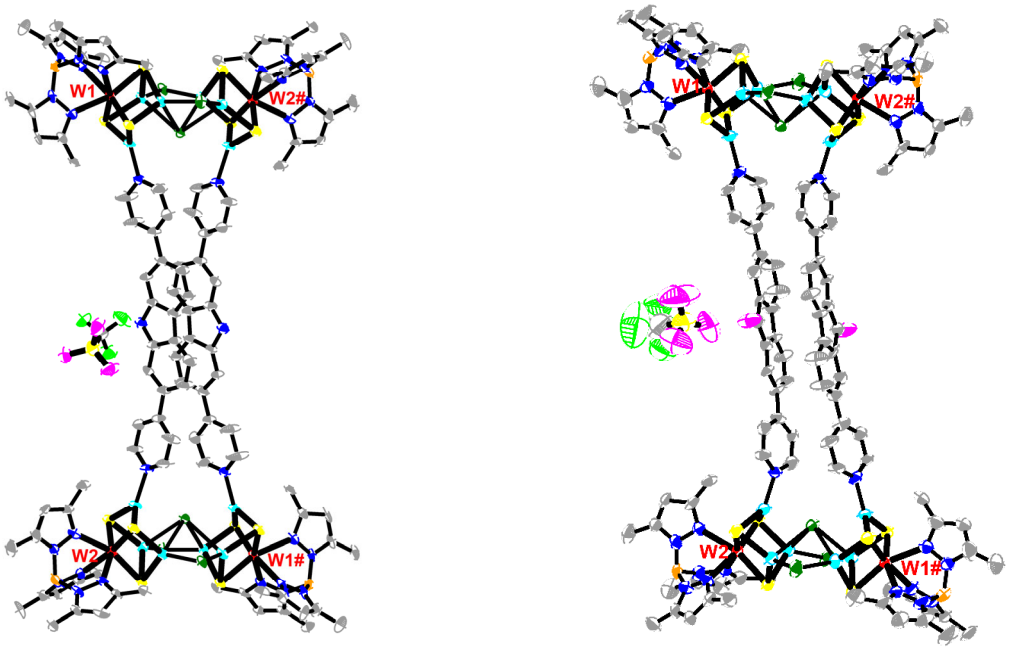

(a) **(b)**

Fig. S7. (a) View of the structure of **4** with all H atoms omitted for clarity. Color codes: W, red; Cu, cyan; S, yellow; Cl, dark green; N, blue; C, black; B, dark orange. (b) View of the structure of **5** with all H atoms omitted for clarity. Color codes: W, red; Cu, cyan; S, yellow; Cl, dark green; N, blue; C, black; B, dark orange; O, Fuchsia.

Details for the third-order NLO measurements of 3-5

Compounds **3**, **4**, and **5** are dissolved in DMF solution with a concentration of 5.0×10^{-5} M and placed in a 1.5 mm quartz cuvette for the third-order NLO measurements. The sample's *Z* position (with respect to the focalpoint at $Z = 0$), the nonlinear absorption [$\alpha = \beta(I_i)$] and the linear absorption α_0 affect the transmittance of light (T) together. The relationship between them is shown in the Eq. 1, where α_0 and α are the linear and effective third-order NLO absorptive coefficients, L is the optical path, and τ is the time.[S3]

$$T(Z) = \frac{\alpha_0}{\sqrt{\pi}\beta I_i(Z)(1-e^{-\alpha_0 L})} \int_{-\infty}^{\infty} \ln\left[1 + \beta I_i(Z)\frac{1-e^{-\alpha_0 L}}{\alpha_0} e^{-\tau^2}\right] d\tau \quad (1)$$

The nonlinear refractive data can be obtained by dividing open-aperture transmittance by closed-aperture transmittance.The peaks and valleys in the nonlinear refraction response spectrum have the same distance from the focus. The trough-peak separation (ΔZ_{V-P}) and the difference between normalized transmittance values at the trough and peak positions (ΔT_{V-P}) fit to the following two equations, which originate for a third-order NLO process (Eq. 2). The effective third-order NLO refractive index n_2 (Eq. 3) can be derived from ΔT_{V-P}, in which α_0, λ, L , and I are the linear coefficient, the wavelength of the laser, the sample thickness, and the peak irradiation intensity at focus, respectively.[S3]

$$\Delta Z_{V-P} = 1.72\pi\omega_0^2/\lambda \quad (2)$$

$$n_2^{eff} = \lambda\alpha_0\Delta T_{V-P}/[0.812\pi I(1-e^{\alpha L})] \quad (3)$$

From β and n_2, the effective third-order NLO susceptibility $\chi^{(3)}$ and the second hyperpolarizability γ values of **3-5** can be obtained through Eqs. 4−7.

$$\chi_I^{(3)} = 9 \times 10^8 \varepsilon_0 n_0^2 c^2 \beta/(4\omega\pi) \quad (4)$$

$$\chi_R^{(3)} = c n_0^2 n_2/(80\pi) \quad (5)$$

$$\chi^{(3)} = \left[(\chi_I^{(3)})^2 + (\chi_R^{(3)})^2\right]^{1/2} \quad (6)$$

$$\gamma = \chi^{(3)}/[N((n_0^2+2)/3)^4] \quad (7)$$

wherein N is the density of the molecules in the unit of number of molecules per cubic centimeters and n_0 is the linear refractive index of DMF ($n_0 = 1.43$). It is noted that the hyperpolarizability γ value can be used to represent the NLO properties of neat materials.

S3 J. F. Ge, Y. T. Lu, R. Sun, J. Zhang, Q. F. Xu, N. J. Li, Y. L. Song and J. M. Lu, *Dyes Pigm.*, 2011, **91**, 489-494.

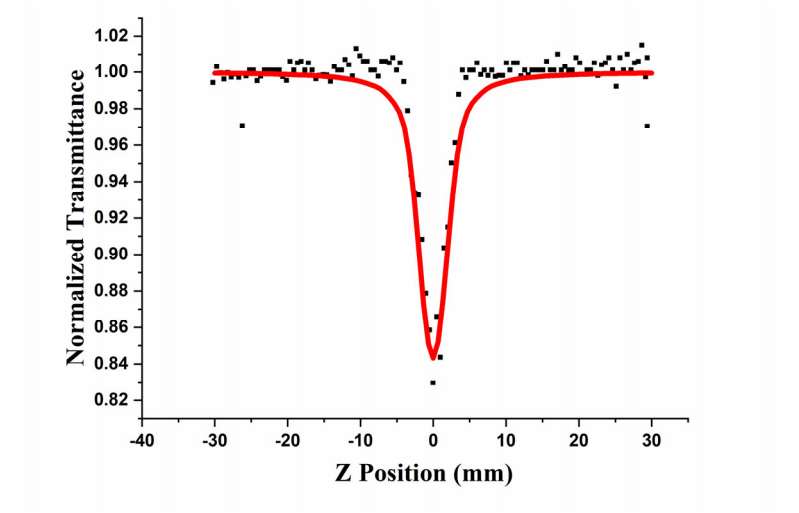

(a)

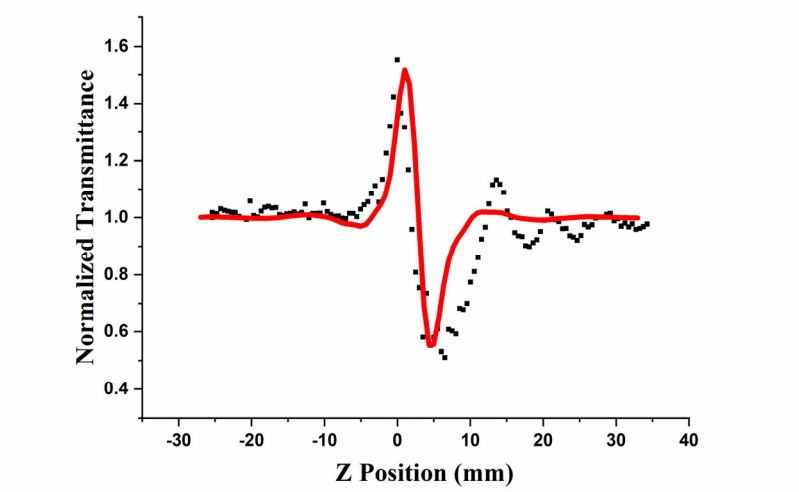

(b)

Fig. S8 *Z*-scan data for **4** (5×10^{-5} M) in DMF investigated at 532 nm. (a) Normalized *Z*-scan data obtained using an open-aperture configuration showing the nonlinear absorption. (b) Normalized *Z*-scan data obtained using a closed-aperture configuration showing the nonlinear refraction. The black solid spheres are the experimental data, and the red solid curves are the theoretical fits.

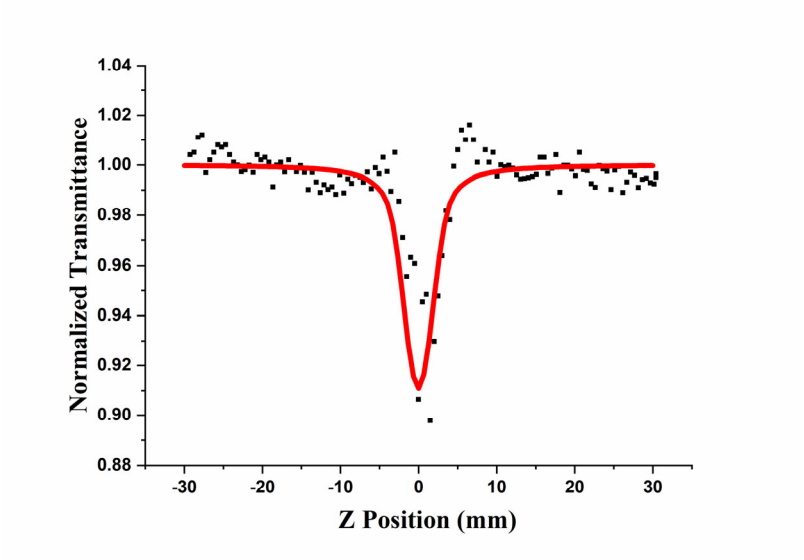

(a)

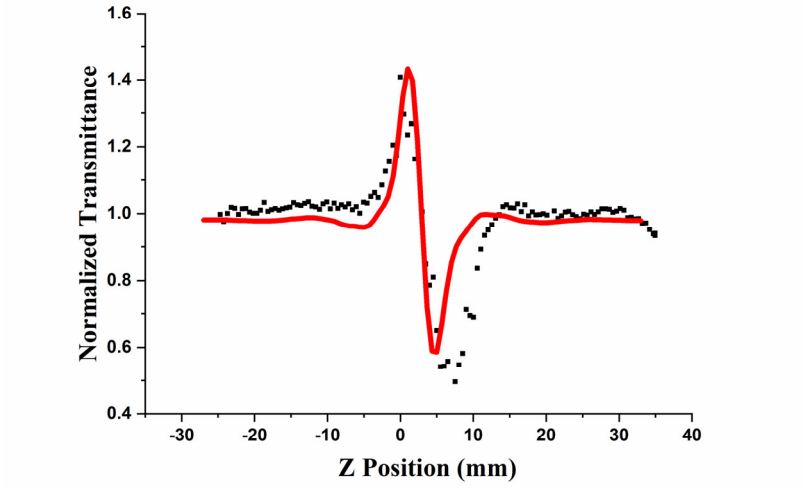

(b)

Fig. S9 *Z*-scan data for **5** (5×10^{-5} M) in DMF investigated at 532 nm. (a) Normalized *Z*-scan data obtained using an open-aperture configuration showing the nonlinear absorption. (b) Normalized *Z*-scan data obtained using a closed-aperture configuration showing the nonlinear refraction. The black solid spheres are the experimental data, and the red solid curves are the theoretical fits.